

October 29, 2018

# First-principles theory of ferroelectric phase transitions for perovskites: The case of BaTiO<sub>3</sub>

W. Zhong and David Vanderbilt

*Department of Physics and Astronomy, Rutgers University, Piscataway, NJ 08855-0849*

K. M. Rabe

*Department of Applied Physics, Yale University, New Haven, CT 06520-8284*

()

## Abstract

We carry out a completely first-principles study of the ferroelectric phase transitions in BaTiO<sub>3</sub>. Our approach takes advantage of two features of these transitions: the structural changes are small, and only low-energy distortions are important. Based on these observations, we make systematically improvable approximations which enable the parameterization of the complicated energy surface. The parameters are determined from first-principles total-energy calculations using ultra-soft pseudopotentials and a preconditioned conjugate-gradient scheme. The resulting effective Hamiltonian is then solved by Monte Carlo simulation. The calculated phase sequence, transition temperatures, latent heats, and spontaneous polarizations are all in good agreement with experiment. We find the transitions to be intermediate between order-disorder and displacive character. We find all three phase transitions

to be of first order. The roles of different interactions are discussed.

77.80.Bh, 61.50.Lt, 64.60.Cn, 64.70.-p

## I. INTRODUCTION

Because of their simple crystal structure, the perovskite oxides present a special opportunity for the development of a detailed theoretical understanding of the ferroelectric phase transition. Within this family of materials, one finds transitions to a wide variety of low-symmetry phases, including ferroelectric and antiferroelectric transitions. Both first- and second-order transitions are observed, with a full spectrum of transition behavior ranging from displacive to order-disorder. The properties of  $\text{BaTiO}_3$ , a much-studied prototypical example of this class of compounds,<sup>1</sup> exemplify this rich behavior.  $\text{BaTiO}_3$  undergoes a succession of first-order phase transitions, from the high-temperature high-symmetry cubic perovskite phase (Fig. 1) to slightly distorted ferroelectric structures with tetragonal, orthorhombic and rhombohedral symmetry. There is increasing evidence that the cubic-to-tetragonal transition, at first thought to be of the simple displacive kind, may instead be better described as of the order-disorder type.

The variety exhibited by the perovskite oxides shows that the phase transformation behavior depends on details of the chemistry and structural energetics of each particular compound. Therefore, it is of the first importance to develop a microscopic theory of the materials properties which determine the ordering of the phases, the character and thermodynamic order of the transitions, and the transition temperatures. The value of a microscopic approach has long been appreciated, but its realization was hindered by the difficulty of determining microscopic parameters for individual compounds. The forms of phenomenological model Hamiltonians<sup>1–4</sup> were limited by the available experimental data, leading to oversimplification and ambiguities in interpretation. For the perovskite oxides, empirical<sup>5</sup> and non-empirical pair potential methods<sup>6</sup> did not offer the high accuracy needed for the construction of realistic models.

First-principles density functional calculations offer an attractive approach for enhancing our microscopic understanding of perovskites and other ferroelectrics. The all-electron Full-potential Linearized-Augmented-Plane-Wave (FLAPW) method has been used by sev-

eral groups to study ferroelectricity in perovskites within the Local Density Approximation (LDA).<sup>7,8</sup> Recently, King-Smith and Vanderbilt performed a systematic study of structural and dynamical properties and energy surfaces for eight common perovskites,<sup>9,10</sup> using the first-principles ultra-soft pseudopotential method and the LDA. These calculations demonstrate that ferroelectricity in the perovskites reflects a delicate balance between long-range electrostatic forces which favor the ferroelectric state, and short-range repulsions which favor the cubic phase. While constrained to calculations of zero-temperature properties, these calculations yield correct predictions of ground state structures and occurrence of ferroelectric phases for certain materials. They show that high-quality LDA calculations can provide considerable insight into the nature of the total-energy surface in the perovskites. For further insight into the energetics of ferroelectric compounds, the polarization generated by various distortions can be studied directly, using a recent first-principles method by King-Smith and Vanderbilt.<sup>11</sup> This approach has been applied to the investigation of the zone-center phonons in the common perovskite oxides.<sup>12</sup>

The application of these first-principles methods can clearly form a foundation for the realistic study of the finite-temperature phase transitions. While an *ab-initio* molecular-dynamics simulation of the structural phase transition is not computationally feasible at present, we pursue an alternative first-principles approach to study ferroelectric phase transitions and demonstrate its application to BaTiO<sub>3</sub>. In particular, we (i) construct an effective Hamiltonian to describe the important degrees of freedom of the system,<sup>13,14</sup> (ii) determine all the parameters of this effective Hamiltonian from high-accuracy *ab-initio* LDA calculations,<sup>9,12,15</sup> and (iii) carry out Monte Carlo (MC) simulations to determine the phase transformation behavior of the resulting system. An abbreviated presentation of this work has already appeared in Ref. 16.

The remainder of this paper is organized as follows. In Sec. II, we go through the detailed procedure for the construction of the effective Hamiltonian, and give the explicit formula. In Sec. III, we describe our first-principles calculations and the determination of the expansion parameters in the Hamiltonian. The technical details of the Monte Carlo simulation are

presented in Sec. IV. In Sec. V, we report our calculated transition temperatures, order parameters, and phase diagram, as well as thermodynamic order and nature of the phase transitions. The role of different interactions in determining the phase transition behavior is also discussed. Sec. VI concludes the paper.

## II. CONSTRUCTION OF THE HAMILTONIAN

### A. Approximations and local modes

The central quantity for studying the equilibrium properties of a system at finite temperature is its partition function. This can be determined from the energy surface, i.e., the total potential energy as a functional of the atomic coordinates. Since the contribution to the partition function decreases exponentially with increasing energy, it is possible to obtain an accurate partition function for low-temperature applications from a simplified energy surface including only low-energy configurations. Our goal is to construct a parameterized Hamiltonian which (i) is *ab initio*, involving no empirical or semi-empirical input; (ii) results in an accurate partition function for the temperature range of interest; (iii) is fully specified by a few *ab initio* total energy calculations; and (iv) involves only approximations that are systematically improvable and removable.

Our first fundamental approximation is to use an energy surface represented by a low-order Taylor expansion. Both experiments and first-principles total energy calculations suggest that the ferroelectric (FE) phase transition involves only very small atomic displacements and strain deformations from the equilibrium cubic structure. It is reasonable to assume that all the atomic configurations with significant contribution to the partition function would be close to this cubic structure in the temperature range of interest. Thus, it is natural to represent the energy surface by a Taylor series in the displacements from the cubic structure. We include up to fourth-order terms in our expansion; this is clearly a minimum, since ferroelectricity is intrinsically an anharmonic phenomenon. By including

higher-order terms, this approximation could later be systematically improved.

It is convenient to describe the small distortions from the cubic structure in terms of the three acoustic and twelve optical normal-mode coordinates per  $k$ -point. While this could be regarded as only a change of basis, it motivates our second fundamental approximation, which is to restrict the expansion to include only low-energy distortions. To achieve this separation, we note that both experimentally-measured and LDA-calculated phonon dispersion relations<sup>1,12</sup> show that only the lowest TO modes (soft modes) and long-wavelength acoustic phonons (strain variables) make significant contributions to the phonon density of states at low energy. Experimental studies also suggest that the FE phase transitions are accompanied by a softening of the lowest TO mode and the appearance of a strain. All other phonons are hardly affected by the transitions. It is then our second approximation to express the energy surface only as a function of the soft-mode amplitudes and strain. This approximation reduces the number of degrees of freedom per cell from fifteen to six, and greatly reduces the number of interaction parameters needed. If necessary, this approximation could later be relaxed by including additional modes.

It is convenient to describe the soft mode over the whole Brillouin zone (BZ) in terms of a collective motion of “local modes,” just as one describes an acoustic phonon in terms of a collective displacement of individual atoms. However, there is more than one choice of local mode which will generate the same soft mode throughout the BZ; an intelligent choice can simplify the Hamiltonian and reduce the number of calculations needed.<sup>17</sup> First, the local mode should be as symmetric as possible, so as to minimize the number of expansion parameters needed. Second, the interactions between local modes at different sites are more difficult to treat than their on-site energy, so the local mode should be chosen so as to minimize intersite interactions. For perovskite  $ABO_3$  compounds, the highest symmetry is achieved by centering the local mode on either atom A or B. In the case of  $BaTiO_3$ , the Ti–O bond is much stronger than the Ba–O bond and the motion of the Ti is more important in the FE transition, so we choose the local mode which is centered on the Ti atom.

The soft zone-center ( $\mathbf{k}=0$ ) FE mode in  $BaTiO_3$  is a  $\Gamma_{15}$  mode which can be characterized

by the four parameters  $\xi_A$ ,  $\xi_B$ ,  $\xi_{O\parallel}$ , and  $\xi_{O\perp}$  (for a mode polarized along the  $j$ 'th Cartesian direction, these refer to the displacements of the A atom, the B atom, the O atom that forms a B–O bond along direction  $j$ , and the other two O atoms, respectively). We take the corresponding local mode to consist of a motion of the central A atom by amount  $\xi_A$ , the eight neighboring B atoms by amounts  $\xi_B/8$ , and the six neighboring O atoms by amounts  $\xi_{O\parallel}/2$  or  $\xi_{O\perp}/2$ , along the  $j$ 'th Cartesian direction. This mode is illustrated in Fig. (1); its amplitude is denoted  $u_j$ . An arbitrary  $k = 0$  soft mode can then be realized as a linear superposition of these local modes having identical amplitudes  $(u_x, u_y, u_z) = \mathbf{u}$  in every cell.

The harmonic interactions between the local-mode amplitudes  $\mathbf{u}_i$  connecting neighboring cells  $i$  must be chosen to reproduce the harmonic behavior of the soft-mode branch throughout the BZ. Long-range Coulomb forces are known to play an important part in these interactions; they are characterized in terms of the calculated Born (or “transverse”) effective charges.<sup>12</sup> Thus, the harmonic intersite interactions are represented by a sum of two contributions: an infinite-range piece that is precisely the interaction of point dipoles whose magnitude is given by the Born effective charge, and corrections which we take to be of covalent origin and therefore local.

To be completely general, anharmonic intercell interactions between neighboring  $\mathbf{u}_i$  would likewise have to be included. Instead, we include only *on-site* anharmonic interactions, which are chosen in such a way that the anharmonic couplings for  $k = 0$  modes of the real system are correctly reproduced. This “local anharmonicity approximation” is an important feature which helps make our scheme tractable and efficient. To go beyond this approximation, one could carry out a careful series of frozen-phonon LDA calculations on supercells to determine anharmonic couplings at other points in the BZ. However, past experience has shown that calculations of this kind are very cumbersome because of the large number of parameters which have to be determined.<sup>18</sup>

With these approximations, our Hamiltonian consists of five parts: a local-mode self energy, a long-range dipole-dipole interaction, a short-range interaction between soft modes, an elastic energy, and an interaction between the local modes and local strain. Symbolically,

$$\begin{aligned}
E^{\text{tot}} = & E^{\text{self}}(\{\mathbf{u}\}) + E^{\text{dpl}}(\{\mathbf{u}\}) + E^{\text{short}}(\{\mathbf{u}\}) \\
& + E^{\text{elas}}(\{\eta\}) + E^{\text{int}}(\{\mathbf{u}\}, \{\eta\}) ,
\end{aligned} \tag{1}$$

where  $\mathbf{u}$  is the local soft-mode amplitude vector, and  $\eta$  is the six-component local strain tensor in Voigt notation ( $\eta_1 = e_{11}$ ,  $\eta_4 = 2e_{23}$ ). In the following subsections, we present the explicit formulae for these five contributions.

### B. Local mode self energy

The first term is

$$E^{\text{self}}(\{\mathbf{u}\}) = \sum_i E(\mathbf{u}_i) , \tag{2}$$

where  $E(\mathbf{u}_i)$  is the energy of an isolated local mode at cell  $\mathbf{R}_i$  with amplitude  $\mathbf{u}_i$ , relative to that of the perfect cubic structure. To describe the FE phase,  $E(\mathbf{u}_i)$  must contain anharmonic as well as harmonic contributions. Since the reference structure is cubic, only even-order terms can enter; we choose to truncate at fourth order. Symmetry considerations then require that it take the form

$$E(\mathbf{u}_i) = \kappa_2 u_i^2 + \alpha u_i^4 + \gamma(u_{ix}^2 u_{iy}^2 + u_{iy}^2 u_{iz}^2 + u_{iz}^2 u_{ix}^2) \tag{3}$$

where  $u_i = |\mathbf{u}_i|$ , and  $\kappa_2$ ,  $\alpha$ , and  $\gamma$  are expansion parameters to be determined from first-principles calculations.

### C. Dipole-dipole interaction

The second term in the effective Hamiltonian represents long-range interactions between local modes. Only dipole-dipole interactions are considered, since higher-order terms tend to be of short range and their effect will be included in the short-range contribution  $E^{\text{short}}(\{\mathbf{u}\})$ . The dipole moment associated with the local mode in cell  $i$  is  $\mathbf{d}_i = Z^* \mathbf{u}_i$ . Here,  $Z^*$  is the Born effective charge for the soft mode, which can be obtained as

$$Z^* = \xi_A Z_A^* + \xi_B Z_B^* + \xi_{O\parallel} Z_{O\parallel}^* + 2\xi_{O\perp} Z_{O\perp}^* \quad (4)$$

from the eigenvector of the soft mode, once the Born effective charges for the ions are known.<sup>12</sup> In atomic units (energy in Hartree), we have

$$E^{\text{dpl}}(\{\mathbf{u}\}) = \frac{Z^*{}^2}{\epsilon_\infty} \sum_{i < j} \frac{\mathbf{u}_i \cdot \mathbf{u}_j - 3(\hat{\mathbf{R}}_{ij} \cdot \mathbf{u}_i)(\hat{\mathbf{R}}_{ij} \cdot \mathbf{u}_j)}{R_{ij}^3}. \quad (5)$$

Here,  $\epsilon_\infty$  is the optical dielectric constant of the material,  $R_{ij} = |\mathbf{R}_{ij}|$ ,  $\mathbf{R}_{ij} = \mathbf{R}_i - \mathbf{R}_j$ , and  $\hat{\mathbf{R}}_{ij} = \mathbf{R}_{ij}/R_{ij}$ .

In practice, Eq. (5) is not directly useful for three-dimensional systems with periodic boundary conditions; instead, we use an Ewald construction to evaluate  $E^{\text{dpl}}$ . We effectively terminate the sum in such a way that the  $k = 0$  modes of the supercell will represent physical TO( $\Gamma$ ) modes. For a TO mode, the induced depolarization electric field is zero; from the point of view of the dipole sum, it is as though the material were surrounded by a layer of metal. In the Ewald construction, this is equivalent to setting the surface terms to zero.<sup>19</sup> Under these conditions, and choosing the decay  $\lambda$  of the Gaussian charge packets to be small enough so that the real-space summation can be entirely neglected, we have

$$E^{\text{dpl}} = \frac{2Z^*{}^2}{\epsilon_\infty} \left[ \frac{\pi}{\Omega_c} \sum_{\mathbf{G} \neq 0} \frac{1}{|\mathbf{G}|^2} \exp\left(-\frac{|\mathbf{G}|^2}{4\lambda^2}\right) \sum_{ij} (\mathbf{G} \cdot \mathbf{u}_i)(\mathbf{G} \cdot \mathbf{u}_j) \cos(\mathbf{G} \cdot \mathbf{R}_{ij}) - \sum_i \frac{\lambda^3 u_i^2}{3\sqrt{\pi}} \right], \quad (6)$$

where  $\Omega_c$  is the cell volume and  $\mathbf{G}$  is the reciprocal lattice vector.

Because of its long-range nature, the calculation of  $E^{\text{dpl}}$  is the most time-consuming part of our Monte Carlo simulations. It is thus worth some special treatment to reduce the computational load. In principle, the term  $R_{ij}$  appearing in the denominator of Eq. (5) should be strain-dependent. However, as we have chosen to expand the intersite interactions between local modes only up to harmonic order, it is consistent to ignore this effect, since strain-induced changes of the dipole-dipole interaction will enter only at higher order. This is equivalent to fixing the reciprocal lattice vectors  $\mathbf{G}$  and all the atomic position vectors  $\mathbf{R}_i$ . The dipole energy can then be written as

$$E^{\text{dpl}} = \sum_{ij,\alpha\beta} Q_{ij,\alpha\beta} u_{i,\alpha} u_{j,\beta}, \quad (7)$$

with

$$Q_{ij,\alpha\beta} = \frac{2Z^{*2}}{\epsilon_\infty} \left[ \frac{\pi}{\Omega_c} \sum_{\mathbf{G} \neq 0} \frac{1}{|\mathbf{G}|^2} \exp\left(-\frac{|\mathbf{G}|^2}{4\lambda^2}\right) \cos(\mathbf{G} \cdot \mathbf{R}_{ij}) G_\alpha G_\beta - \frac{\lambda^3}{3\sqrt{\pi}} \delta_{\alpha\beta} \delta_{ij} \right]. \quad (8)$$

Here,  $\alpha$  and  $\beta$  denote Cartesian components. The matrix  $Q$  is thus treated as a constant; it is calculated once and for all, and stored for later calculation of the dipole energy. This strategy increases the computational efficiency by at least one order of magnitude.

#### D. Short-range interaction

$E^{\text{short}}(\{\mathbf{u}\})$  is the energy contribution due to the short-range interactions between neighboring local modes, with dipole-dipole interaction excluded. This contribution stems from differences of short-range repulsion and electronic hybridization between two adjacent local modes and two isolated local modes. Together with the dipole-dipole interaction, this interaction determines the soft-mode energy away from the zone center. Expanded up to the second order, it can be written as,

$$E^{\text{short}}(\{\mathbf{u}\}) = \frac{1}{2} \sum_{i \neq j} \sum_{\alpha\beta} J_{ij,\alpha\beta} u_{i\alpha} u_{j\beta}. \quad (9)$$

The coupling matrix  $J_{ij,\alpha\beta}$  is a function of  $\mathbf{R}_{ij}$  and should decay very fast with increasing  $|\mathbf{R}_{ij}|$ . Here, we consider the short-range interaction up to third nearest neighbor (nn), whose local mode shares atoms with the local mode on the origin. Local modes between further neighbors involve displacements of atoms at least two hops away (in tight-binding language) and their core-core repulsion or hybridization should be much less important than the dipole-dipole interaction which is taken care of in  $E^{\text{dpl}}$ .

The interaction matrix  $J_{ij,\alpha\beta}$  can be greatly simplified by symmetry. For a cubic lattice, we have,

$$\begin{aligned} \text{1st nn : } J_{ij,\alpha\beta} &= (j_1 + (j_2 - j_1)|\hat{R}_{ij,\alpha}|) \delta_{\alpha\beta}, \\ \text{2nd nn : } J_{ij,\alpha\beta} &= (j_4 + \sqrt{2}(j_3 - j_4)|\hat{R}_{ij,\alpha}|) \delta_{\alpha\beta} \\ &\quad + 2j_5 \hat{R}_{ij,\alpha} \hat{R}_{ij,\beta} (1 - \delta_{\alpha\beta}), \\ \text{3rd nn : } J_{ij,\alpha\beta} &= j_6 \delta_{\alpha\beta} + 3j_7 \hat{R}_{ij,\alpha} \hat{R}_{ij,\beta} (1 - \delta_{\alpha\beta}), \end{aligned} \quad (10)$$

where  $\hat{R}_{ij,\alpha}$  is the  $\alpha$  component of  $\mathbf{R}_{ij}/R_{ij}$ . So we have only seven interaction parameters for a cubic lattice. The coefficients  $j_1, j_2, \dots, j_7$  in the above equations have physical meanings that are sketched schematically in Fig. 2. For example,  $j_1$  represents the interaction strength of “ $\pi$ ” like interactions between first neighbors.

### E. Elastic energy

We will describe the state of elastic deformation of the BaTiO<sub>3</sub> crystal using local strain variables  $\eta_l(\mathbf{R}_i)$ , where the Voigt convention is used ( $l = 1, \dots, 6$ ) and  $\mathbf{R}_i$  labels a cell center (Ti) site. In fact, the six variables per unit cell  $\{\eta_l(\mathbf{R}_i)\}$  are not independent, but are obtained from three independent displacement variables per unit cell. In our analysis, these are taken as the dimensionless displacements  $\mathbf{v}(\mathbf{R}_i)$  (in units of the lattice constant  $a$ ) defined at the unit cell corner (Ba) positions  $\mathbf{R}_i + (a/2, a/2, a/2)$ . In terms of these, the *inhomogeneous* strain variables  $\eta_{l,l}(\mathbf{R}_i)$  are defined in the next subsection. Because of our use of a periodic supercell in the Monte Carlo simulations, however, homogeneous strain deformations are not included in the configuration space  $\{\mathbf{v}(\mathbf{R}_i)\}$ . Therefore, we introduce six additional *homogeneous* strain components  $\eta_{H,l}$  to allow the simulation cell to vary in shape. The total elastic energy is expanded to quadratic order as

$$E^{\text{elas}}(\{\eta_l\}) = E_{\text{I}}^{\text{elas}}(\{\eta_{l,l}\}) + E_{\text{H}}^{\text{elas}}(\{\eta_{H,l}\}), \quad (11)$$

where the homogeneous strain energy is simply given by

$$\begin{aligned} E_{\text{H}}^{\text{elas}}(\{\eta_{H,l}\}) &= \frac{N}{2} B_{11} (\eta_{H,1}^2 + \eta_{H,2}^2 + \eta_{H,3}^2) \\ &+ N B_{12} (\eta_{H,1} \eta_{H,2} + \eta_{H,2} \eta_{H,3} + \eta_{H,3} \eta_{H,1}) \\ &+ \frac{N}{2} B_{44} (\eta_{H,4}^2 + \eta_{H,5}^2 + \eta_{H,6}^2). \end{aligned} \quad (12)$$

Here  $B_{11}$ ,  $B_{12}$ , and  $B_{44}$  are the elastic constants expressed in energy units ( $B_{11} = a^3 C_{11}$ , etc.), and  $N$  is the number of primitive cells in the supercell.

Rather than use an expression like (12) for the inhomogeneous strain energy, we have found it preferable to express this part directly in terms of the  $\mathbf{v}(\mathbf{R}_i)$ .<sup>20</sup> This approach keeps

the acoustic phonon frequencies well behaved throughout the Brillouin zone. To satisfy requirements of invariance under translations and rotations of the crystal as a whole, the energy is expanded in scalar products of differences between the  $\mathbf{v}(\mathbf{R}_i)$ . The cubic crystal symmetry leads to a great reduction of the independent parameters in the expansion. The energies of the long-wavelength strain deformations can be reproduced by an expansion of the form

$$\begin{aligned}
E_I^{\text{elas}} = & \sum_i \left\{ \gamma_{11} [v_x(\mathbf{R}_i) - v_x(\mathbf{R}_i \pm \mathbf{x})]^2 \right. \\
& + \gamma_{12} [v_x(\mathbf{R}_i) - v_x(\mathbf{R}_i \pm \mathbf{x})] [v_y(\mathbf{R}_i) - v_y(\mathbf{R}_i \pm \mathbf{y})] \\
& + \gamma_{44} [v_x(\mathbf{R}_i) - v_x(\mathbf{R}_i \pm \mathbf{y}) + v_y(\mathbf{R}_i) - v_y(\mathbf{R}_i \pm \mathbf{x})]^2 \\
& \left. + \text{cyclic permutations} \right\} \quad (13)
\end{aligned}$$

corresponding to bond stretching, bond correlation, and bond bending, respectively. Here,  $\mathbf{x} \equiv a\hat{\mathbf{x}}$ ,  $\mathbf{y} \equiv a\hat{\mathbf{y}}$ ,  $\mathbf{z} \equiv a\hat{\mathbf{z}}$ , and  $\pm$  indicates multiple terms to be summed. The  $\gamma$  coefficients are related to the elastic constants by  $\gamma_{11} = B_{11}/4$ ,  $\gamma_{12} = B_{12}/8$ , and  $\gamma_{44} = B_{44}/8$ .

## F. Elastic-mode interaction

To describe the coupling between the elastic deformations and the local modes, we use the on-site interaction

$$E^{\text{int}}(\{\mathbf{u}\}, \{\eta_l\}) = \frac{1}{2} \sum_i \sum_{l\alpha\beta} B_{l\alpha\beta} \eta_l(\mathbf{R}_i) u_\alpha(\mathbf{R}_i) u_\beta(\mathbf{R}_i) . \quad (14)$$

As a result of cubic symmetry, there are only three independent coupling constants  $B_{l\alpha\beta}$ :

$$\begin{aligned}
B_{1xx} &= B_{2yy} = B_{3zz} , \\
B_{1yy} &= B_{1zz} = B_{2xx} = B_{2zz} = B_{3xx} = B_{3yy} , \\
B_{4yz} &= B_{4zy} = B_{5xz} = B_{5zx} = B_{6xy} = B_{6yx} .
\end{aligned}$$

The strain contains both homogeneous and inhomogeneous parts.  $\eta_l(\mathbf{R}_i) = \eta_{\text{H},l}(\mathbf{R}_i) + \eta_{\text{I},l}(\mathbf{R}_i)$ . The latter are expressed in terms of the local displacement vectors  $\mathbf{v}$  as follows. We first define the six average differential displacements associated with site  $\mathbf{R}_i$  as

$$\Delta v_{xx} = \sum_{\mathbf{d}=0,\mathbf{y},\mathbf{z},\mathbf{y}+\mathbf{z}} [v_x(\mathbf{R}_i - \mathbf{d} - \mathbf{x}) - v_x(\mathbf{R}_i - \mathbf{d})] ,$$

$$\Delta v_{xy} = \sum_{\mathbf{d}=0,\mathbf{y},\mathbf{z},\mathbf{y}+\mathbf{z}} [v_y(\mathbf{R}_i - \mathbf{d} - \mathbf{x}) - v_y(\mathbf{R}_i - \mathbf{d})] ,$$

and their cyclic permutations, recalling that  $\mathbf{v}(\mathbf{R}_i)$  is associated with position  $\mathbf{R}_i + (a/2, a/2, a/2)$ . Then  $\eta_{l,1}(\mathbf{R}_i) = \Delta v_{xx}/4$ ,  $\eta_{l,4}(\mathbf{R}_i) = (\Delta v_{yz} + \Delta v_{zy})/4$ , etc.

### III. FIRST-PRINCIPLES CALCULATIONS

We have shown that, with the two approximations we made, the total energy functional of the perovskite system is fully specified by a set of parameters. These parameters can be obtained from first-principles calculations. We use density-functional theory within the local density approximation (LDA). The technical details and convergence tests of the calculations can be found in Refs. 9,10. The most important feature of the calculations is the Vanderbilt ultra-soft pseudopotential,<sup>15</sup> which allows a low energy cutoff to be used for first-row elements. This makes high-accuracy large-scale calculations of materials involving oxygen and *3d* transition metal elements affordable. The ultra-soft pseudopotential also allows for exceptionally transferable pseudopotentials. It ensures that all-electron and pseudo-atom scattering properties agree over a very large energy range and preserves the chemical hardness of the atom. A generalized Kohn-Sham functional is directly minimized using a preconditioned conjugate gradient method.<sup>10,21,22</sup> We use a (6,6,6) Monkhorst-Pack k-point mesh<sup>23</sup> for single-cell calculations, i.e., 216 k-points in the full Brillouin zone (FBZ). For supercell calculations, the k mesh is kept the same to minimize errors due to the k-point sampling. Therefore, a smaller number of k-points is used because of the smaller FBZ.

We start with the construction of the local mode vectors. All the eigenvalues and eigenvectors of the force-constant matrix at  $k = 0$  for the cubic  $\text{BaTiO}_3$  structure are calculated from frozen-phonon calculations, as in Ref. 10. The mode with imaginary frequency is identified as the soft mode. The soft-mode eigenvector has been reported previously<sup>10</sup> as  $\xi_{\text{Ba}} = 0.20$ ,  $\xi_{\text{Ti}} = 0.76$ ,  $\xi_{\text{O}\parallel} = -0.53$ , and  $\xi_{\text{O}\perp} = -0.21$ . The local mode is then constructed from it using the scheme proposed in II.1 (Fig.1).

Determination of many of the parameters in the effective Hamiltonian involves only calculations for zone-center distortions. These parameters have been reported previously.<sup>10,12</sup> They include the fourth-order terms of on-site energy  $\alpha$  and  $\gamma$ ; the elastic constants  $B_{11}, B_{12}, B_{44}$ ; and the on-site elastic-mode interaction parameters  $B_{1xx}, B_{1yy}, B_{4yz}$ . The mode effective charge  $Z^*$  of Eq. (4) is calculated from the values  $Z_A^*=2.75$ ,  $Z_B^*=7.16$   $Z_{O\parallel}^*=-5.69$ , and  $Z_{O\perp}^*=-2.11$  published in Ref. 12. (The resulting value  $Z^*=9.96$  is slightly different from the one given in Ref. 12; there, the eigenvector of the *dynamical* matrix, not the *force-constant* matrix, was used.) We use the experimental value  $\epsilon_\infty = 5.24$  of the optical dielectric constant, since for this quantity, the LDA seems not to be a well-justified approximation, while exact density-functional theory results are not accessible. We find, however, that the effect of a small inaccuracy in the dielectric constant affects thermodynamic properties such as transition temperatures only slightly.

The second-order energy parameter  $\kappa$  for zone-center distortions is a linear combination of the local mode self energy parameter  $\kappa_2$ , the intersite interactions  $j_i$ , and the dipole-dipole interaction. The calculations of intersite interaction parameters involve determination of the energy for distortions at the zone-boundary k-points  $X=(\pi/a,0,0)$ ,  $M=(\pi/a,\pi/a,0)$ , and  $R=(\pi/a,\pi/a,\pi/a)$ , where  $a$  is the lattice constant. Five frozen-phonon calculations on doubled unit cells are sufficient to extract all the information available from these k-points. The arrangement of the local mode vectors for each case, as well as for the zone-center distortion at  $\Gamma=(0,0,0)$ , are shown in Fig. 3. The actual ionic configurations are constructed by superpositions of displacements associated with adjacent local modes. For example, letting  $u$  be the amplitude of the Ti-centered local mode defined in Sec. II A, the displacement of the Ti atoms is just  $u\xi_{\text{Ti}}$  in Fig. 3(a) and  $\pm u\xi_{\text{Ti}}$  in Fig. 3(b), while Ba is affected by eight neighboring local modes so that its displacement is  $8 \times u\xi_{\text{Ba}}/8 = u\xi_{\text{Ba}}$  in Fig. 3(a) and 0 in Fig. 3(b).

The above five doubled-cell calculations can be used to determine the parameters  $j_1$ ,  $j_2$ ,  $j_3$ ,  $j_4$ , and  $j_6$ . The determination of  $j_5 + 2j_7$  requires a four-cell calculation involving 20 atoms with low symmetry [Fig. 3(g)]. Table I lists the energy expressions for all the

configurations calculated in terms of the quadratic expansion parameters.

A further decomposition of  $j_5$  and  $j_7$  would require an expensive eight-cell calculation. Furthermore, the interaction parameter  $j_7$  is the third nearest-neighbor interaction and is thus presumably not very important. This argument is justified by our Monte Carlo simulations which show that the calculated transition temperature is insensitive to different decompositions of  $j_5$  and  $j_7$ . This prompts us to make an approximate decomposition based on a simple physical argument: we expect the interaction to be smallest for two interacting local modes oriented such that reversing the relative sign of the vectors produces the least change of bond lengths. Applied to third nearest neighbors, this argument implies  $j_6 - 2j_7 = 0$ , thus fixing the value of  $j_7$ .

The resulting interaction parameters are shown in Table II, together with other parameters published previously. It may be surprising to see that the on-site  $\kappa_2$  is positive, while the cubic structure is known to be unstable against  $k = 0$  distortion. The cubic structure is thus stable against forming an isolated local mode; instability actually comes from the intersite interactions between local modes. To be more precise, we find that it is the long-range Coulomb (dipole-dipole) interaction which makes the ferroelectric state favorable. If we turn off the dipole-dipole interaction by setting the effective charge  $Z^* = 0$ , we find that the ferroelectric instability disappears. This is consistent with the previous point of view that long-range Coulomb forces favor the ferroelectric state, while short-range repulsions favor the nonpolar cubic state.

From Table II, we see that the intersite interaction parameters decay very fast with increasing distance, indicating the short-range nature of the intersite interactions after the long-range Coulomb interactions have been separated out. The ratio of the magnitudes of the strongest first-, second-, and third-neighbor interactions turns out to be approximately  $1 : 0.23 : 0.09$ . This decays even faster than the dipole-dipole interactions, for which the corresponding ratio ( $\propto 1/R^3$ ) is  $1 : 0.35 : 0.19$ . These results help justify our approximation of including only up to third nearest neighbors for the short-range interactions.

#### IV. MONTE CARLO SIMULATIONS

For the quantitative study of non-universal finite-temperature behavior of a given model, Monte Carlo simulation<sup>19,24</sup> has emerged as the most reliable and powerful technique. It is especially appropriate for a model such as ours, with two continuous vector degrees of freedom per unit cell and both short and long range interactions, for which analytical approaches such as renormalization group or high-temperature expansions would be cumbersome and involve additional approximations. In comparison, the Monte Carlo approach requires only the ability to compute changes in total energy as the configuration is changed. Furthermore, with suitable analysis of statistical errors and finite-size effects, the results of Monte Carlo simulation can be made arbitrarily accurate. Finally, with little additional effort, a number of physical quantities can be computed to aid in characterization of the transition.

We solve the effective Hamiltonian [Eqs. (2), (7), (9), (11), and (14)] using Monte Carlo simulations with the Metropolis algorithm<sup>25</sup> on an  $L \times L \times L$  cubic lattice with periodic boundary conditions. Since most energy contributions (except  $E^{\text{dpl}}$ ) are local, we choose the single-flip algorithm. That is, a trial move consists of an attempted update of a single variable, after which the total energy change is calculated to determine whether to accept the move. The step sizes are adjusted to ensure an acceptance ratio of approximately 0.2. In one Monte Carlo sweep (MCS), we first make a trial move on each  $\mathbf{u}_i$  in sequence, then each  $\mathbf{v}_i$  in sequence, then iterate several times (typically  $2L$  times) on the homogeneous strain variables. For  $L = 12$ , each MCS takes about one second on an HP 735 workstation. The typical correlation time for the total energy is found to be several hundred MCS close to the phase transition; this long correlation time makes certain new MC techniques using energy distribution functions<sup>26</sup> unfavorable. The correlation times for the local mode amplitudes are one order of magnitude shorter, and thus 10,000 MCS are usually enough to equilibrate and to obtain averages of local mode variables with statistical error  $< 10\%$ .

In our simulation, we concentrate on identifying the succession of low-temperature phases, determining the phase transition temperatures, and extracting qualitative features

of the transitions. This analysis will allow us to identify the features of the effective Hamiltonian which most strongly affect the transition properties. For these purposes, it is most convenient to monitor directly the behavior of the homogeneous strain and the vector order parameter. In the case of the ferroelectric phase transition, the latter is just the average local-mode vector  $\mathbf{u} = \sum_i \mathbf{u}_i / N$ , which is proportional to the polarization. Here,  $\mathbf{u}_i$  is the local mode vector at site  $i$  and  $N$  is the total number of sites. As a reference, the average local mode amplitude  $u = \sum_i |\mathbf{u}_i| / N$  is also monitored. To avoid effects of symmetry-equivalent rotations of the order parameter and to identify the different phases clearly, we accumulate the absolute values of the largest, middle, and smallest components of the averaged local-mode vector for each step, denoted by  $u_1$ ,  $u_2$ , and  $u_3$ , respectively ( $u_1 > u_2 > u_3$ ). The cubic (C), tetragonal (T), orthorhombic (O), and rhombohedral (R) phases are then characterized by zero, one, two, and three non-zero order-parameter components, respectively. The effect of symmetry-equivalent rotations on the homogeneous strain is handled analogously, with the largest, the medium and the smallest linear strain components denoted by  $\eta_1$ ,  $\eta_2$  and  $\eta_3$ , respectively, and shear strain components by  $\eta_4$ ,  $\eta_5$  and  $\eta_6$ .

The ferroelectric phase transition is very sensitive to hydrostatic pressure, or equivalently, to lattice constant. The LDA-calculated lattice constants are typically 1% too small, and even this small error can lead to large errors in the zero-pressure transition temperatures. One approach which largely compensates for the effect of this systematic error is to exert a negative pressure that expands the lattice constant to the experimental value. We determine the value of the pressure by calculating volumes for four different phases and comparing with experimental measurements.<sup>27</sup> We find  $P = -4.8$  GPa gives the best overall agreement (although the application of pressure does lead to a slight change in the low temperature structure). Except for the simulations for the construction of the temperature-pressure phase diagram, the following simulations and analysis are for this pressure.

## V. RESULTS AND DISCUSSION

In this section, the finite-temperature behavior of the model is presented and analyzed. First, we examine the order parameters as a function of temperature in a typical simulation to obtain a measure of the transition temperatures. From the results of simulations for a range of pressures, we construct the temperature-pressure phase diagram. For the system at ambient pressure, more detailed simulations are performed. The order of the transitions, the nature of the paraelectric phase and the properties of the low-temperature phases are investigated and compared with experimental observations. Finally, the roles played by different terms in the effective Hamiltonian and the sensitivity of the results to various approximations are examined.

### A. Order parameters and phase diagram

We start the simulations at a high temperature ( $T > 400\text{K}$ ) and equilibrate for 10,000 MCS. The temperature is then reduced in small steps, typically 10K. After each step, the system is allowed to equilibrate for 10,000 MCS. The order parameter averages are then accumulated over a period of 7,000 MCS, yielding a typical standard deviation of less than 10%. The temperature step size is reduced and the number of MCS is doubled for temperatures close to the phase transition.

Fig. 4 shows the averaged local-mode vectors  $u_1$ ,  $u_2$ ,  $u_3$  and averaged local mode amplitude  $u$  as functions of temperature in a typical simulation for an  $L = 12$  lattice at  $P = -4.8$  GPa. At high temperatures,  $u_1$ ,  $u_2$ , and  $u_3$  are all very close to zero. As the system is cooled down below 295K,  $u_1$  increases and becomes significantly larger than  $u_2$  or  $u_3$ . This indicates the transition to the tetragonal phase. Two additional phase transitions occur as the temperature is reduced further. The T–O transition (sudden increase of  $u_2$ ) occurs at 230K and the O–R transition (sudden increase of  $u_3$ ) occurs at 190K. The sequence of transitions exhibited by the simulation is the same as that observed experimentally.

The averaged homogeneous strain variables obtained from the above simulation are shown in Fig. 5. These strains are measured relative to the LDA calculated equilibrium cubic structure, so the linear strains are significantly non-zero at higher temperatures due to the negative pressure applied. As expected, the simulation cell changes shape at the same temperatures at which the jumps of order parameter components are observed. At high temperatures, we have approximately  $\eta_1 = \eta_2 = \eta_3$  and  $\eta_4 = \eta_5 = \eta_6 = 0$ , corresponding to the cubic structure. As the system is cooled down, the shape of the simulation cell changes to T, O, and R phases. The orthorhombic (O) structure has a non-zero shear strain, in agreement with the centered orthorhombic structure observed experimentally. Quantitatively, our calculated distortions are also in good agreement with the experiment, with the calculated distortions tending to be slightly smaller. For example,  $\eta_1 - \eta_3$  for the tetragonal phase is 1.1% as measured from experiment<sup>27</sup> and 0.9% from our calculation.

The simulations are repeated for a range of applied pressures to obtain the temperatures at which the order parameter components and homogeneous strain jump on cooling down. The resulting temperature-pressure phase diagram is shown in Fig. 6. (This measure of the transition temperature is actually a lower bound, due to hysteresis around 5% for T–O and O–R transitions and negligible for the C–T transition, to be discussed further below.) All three transition temperatures decrease almost linearly with increasing pressure. At the experimental lattice constant, the values for  $dT_c/dP$  are found to be  $-28$ ,  $-22$ , and  $-15$  K/GPa for the C–T, T–O, and O–R transitions respectively. The experimental values for the C–T transition range from  $-40$  K/GPa<sup>28</sup> to  $-66$  K/GPa.<sup>29</sup> For the T–O transition the measured value is  $-28$  K/GPa,<sup>29</sup> and for the O–R transition it is  $-10$  to  $-15$  K/GPa.<sup>29</sup> At pressures as high as  $P = 5$  GPa, the sequence of phases C–T–O–R is still observed in the simulation. When the pressure is increased further, the phase boundary in the simulation becomes unclear due to fluctuations. Our calculated critical pressure (beyond which the cubic structure is stable at  $T=0$  K) is  $P_c = 8.4$  GPa. Taking into account the pressure correction for the LDA volume underestimate, this corresponds to a predicted physical  $P_c = 13.2$  GPa. We are not aware of any experimental value for  $P_c$  with which to compare

this value. However, we find that the magnitude of our  $dT_c/dP$  is significantly smaller than experimental value, at least for the C–T and T–O transitions. This may partly be due to the neglect of higher-order strain coupling terms in the effective Hamiltonian. We have tested the effect of including a volume dependence for the short-range interaction parameters  $j_i$ . This correction does not change the sequence of phases, and it only increases the magnitudes of  $dT_c/dP$  slightly. Therefore, our results are reported without this correction. The accuracy of the phase diagram may be further improved by including higher-order terms in the elastic energy, or the coupling of  $j_i$  to anisotropic strain.

### B. Hysteresis and latent heat

For the investigation of the order of the transitions, the nature of the paraelectric phase and the properties of the low-temperature phases, we performed more detailed simulations at  $P = -4.8\text{GPa}$  for the three system sizes  $L = 10, 12$  and  $14$ . In the cooling-down simulations, the length of each simulation was increased from 10,000 to up to 35,000 MCS at temperatures close ( $\pm 10\text{K}$ ) to the phase transition to include a longer equilibration. The size of the temperature step was decreased to 5K or less in the vicinity of the transition. In addition, a heating simulation was performed, starting from the lower-temperature phase, to detect any possible hysteresis. The calculated transition temperatures, obtained as the average of the cooling and heating transition temperatures, are given in Table III. The error estimates in the table are determined by the width of the hysteresis, which persists even for the longest simulation lengths considered. (The C–T transition temperature for  $L = 10$  is difficult to identify because of large fluctuations between phases.) The calculated transition temperatures are well converged with respect to system size, and are in reasonable agreement with experiment. Table III also gives the saturated spontaneous polarization  $p_s$  at  $T = 0$  in the R phase, and just above the O–R and T–O transitions in the O and T phases respectively. These are calculated from the average local mode vector  $\mathbf{u}$  and the local mode  $Z^*$ . We find almost no finite-size effect for this quantity, and the agreement with experiment

is very good for the O and T phases. The disagreement for the R phase may result in part from twinning effects in the experimental sample.<sup>30</sup>

From the jumps in structural parameters and the observed hysteresis in heating and cooling, we conclude that the phase transitions are first order. An accurate determination of the latent heats would require considerable effort;<sup>31</sup> here, we only try to provide estimates sufficiently accurate for meaningful comparison with experiment. We approach each transition from both high-temperature and low-temperature sides until the point is reached where both phases appear equally stable. (That is, the typical time for the system to fluctuate into the opposite phase is roughly independent of which phase the simulation is started in.) The difference of the average total energy is then the latent heat.<sup>32</sup> This approach is practical as long as some hysteresis is present. The calculated latent heats (Table III) show non-negligible finite-size dependence. Taking this into account, we find that the latent heats for all three transitions are significantly non-zero and in rough agreement with the rather scattered experimental data. For the T–O and O–R transitions, the first-order character of the transition is predicted by Landau theory, since in these two cases the symmetry group of the low temperature structure is not a subgroup of that of the high temperature structure. For the C–T transition, the first-order character is not a consequence of symmetry, but rather of the values of the effective Hamiltonian parameters. Although it has the largest latent heat of the three transitions, the C–T transition also exhibits large finite-size effects in the latent heat and in the smearing of order parameter components and strain discontinuities in the simulation (Figs. 4,5). This suggests the presence of long-wavelength fluctuations characteristic of second-order phase transitions and critical phenomena, and the classification of the C–T transition as a weak first-order transition.

### C. Displacive vs. order-disorder

Using the microscopic information available in the simulations, we are able to investigate the extent to which the cubic-tetragonal transition can be characterized as order-disorder

or displacive. These possibilities can be distinguished by inspecting the distribution of the real-space local-mode vector  $\mathbf{u}_i$  in the cubic phase just above the transition. A displacive (microscopically nonpolar) or order-disorder (microscopically polar) transition should be characterized by a single-peaked or double-peaked structure, respectively. The distribution of  $u_x$  at  $T = 400\text{K}$  is shown in Fig. 7. It exhibits a rather weak tendency to a double-peaked structure, indicating a transition which has some degree of order-disorder character. We also see indications of this in the  $u$ - $T$  relation in Fig. 4. Even in the cubic phase, the average of the local-mode magnitude  $u$  is significantly non-zero and close to that of the rhombohedral phase, while the magnitudes of the average local mode components change dramatically during the phase transitions.

In reciprocal space, a system close to a displacive transition should show large and strongly temperature-dependent fluctuations of certain modes associated with a small portion of the Brillouin zone (BZ) (for a ferroelectric transition, near  $\Gamma$ ). For an extreme order-disorder transition, on the other hand, the fluctuations are expected to be distributed over the whole BZ. For  $\text{BaTiO}_3$ , we calculated the average Fourier modulus  $F(\mathbf{k}, T) = \langle |u(\mathbf{k})|^2 \rangle$  for eigenmodes at several high-symmetry k-points (along  $\Gamma$ -X,  $\Gamma$ -M and  $\Gamma$ -R) for a range of temperatures above the C-T transition. These eigenmodes are identified by their symmetry properties as one longitudinal optical (LO) branch and two transverse optical (TO) branches at each point. For a purely harmonic system,  $T/F(\mathbf{k}, T)$  can be shown to be a temperature-independent constant proportional to the square of the eigenfrequency  $\omega^2(\mathbf{k})$  of the corresponding eigenmode. A strong decrease of  $T/F(\mathbf{k}, T)$  as  $T \rightarrow T_c$  from high temperature can be interpreted as mode softening due to anharmonicity.

The results at the k-point  $(\pi/4a, \pi/4a, 0)$  illustrate the main features of this analysis. From symmetry, three nondegenerate eigenmodes LO, TO1, TO2 are identified. The polarization of LO, TO1, and TO2 are in the direction of  $\hat{\mathbf{x}} + \hat{\mathbf{y}}$ ,  $\hat{\mathbf{x}} - \hat{\mathbf{y}}$ , and  $\hat{\mathbf{z}}$ , respectively. For each eigenmode, the temperature dependence of the calculated  $\omega^2(\mathbf{k}, T)$  is shown in Fig. 8. The almost linear behavior of  $\omega^2(\mathbf{k}, T)$  vs.  $T$  (the Curie-Weiss form) is observed for the other k-points as well. Both the LO and TO1 branches are almost temperature independent. The

TO2 branch is strongly temperature dependent and is thus a “soft” mode. According to the soft-mode theory of structural phase transitions,  $T_c$  is the lowest temperature at which all  $\omega^2(\mathbf{k}, T) \geq 0$ . Linear extrapolation indicates that the TO2 mode frequency goes to zero at  $T \approx 200\text{K}$ , which is a lower bound for  $T_c$ , consistent with the value obtained in Monte Carlo simulations. A similar calculation of  $\omega^2(\mathbf{k}, T)$  for the TO modes at  $\Gamma=(0,0,0)$  extrapolates to zero at the higher temperature  $T \approx 300\text{K}$ , in excellent agreement with the Monte Carlo value of 295K.

Within this formalism, the microscopic character of the paraelectric phase is determined by the extent of the soft mode in the BZ. We define a quantity

$$\rho(\mathbf{k}) = \frac{2F(\mathbf{k}, 350\text{K})}{F(\mathbf{k}, 700\text{K})} \quad (15)$$

to indicate the hardness of the modes. In Fig. 9,  $\rho(\mathbf{k})$  is shown for the various k-points along some special directions in the BZ. If  $\rho(\mathbf{k}) < 1$ , the corresponding eigenfrequency extrapolates to zero at some positive temperature, and the mode is regarded as soft. If  $\omega^2(\mathbf{k})$  is independent of temperature,  $\rho(\mathbf{k}) = 2$ , corresponding to the hardest mode.

For all the k-points considered, all the LO modes are almost temperature independent [ $\rho(\mathbf{k}) = 2$ ] and are not included in the figure. Along the  $\Gamma$ –X direction, the doubly-degenerate TO modes are soft all the way to the zone boundary. In contrast, along the  $\Gamma$ –R direction, both TO modes become hard immediately after leaving the  $\Gamma$  point. Along the  $\Gamma$ –M direction, the TO1 mode becomes hard quickly, while the TO2 branch remains soft at least halfway to the zone boundary. This behavior, especially along  $\Gamma$ –X, does not conform completely to the displacive limit. This supports the interpretation of the C–T transition as intermediate between displacive and order-disorder, with a slightly stronger order-disorder character. Thus, from the example of BaTiO<sub>3</sub>, it seems that a positive on-site quadratic coefficient does not automatically imply a displacive character for the transition. Rather, the relevant criterion is the extent to which the unstable modes extend throughout the BZ.

## D. Roles of different interactions

Our theoretical approach allows us to investigate the roles played by different types of interaction in the phase transition. First, we study the effect of strain. Recall that the strain degrees of freedom were separated into local and homogeneous parts, representing finite- and infinite-wavelength acoustic modes, respectively. Both parts were included in the simulations. If we eliminate the local strain (while still allowing homogeneous strain), we find almost no change in the transition temperatures. This indicates that the effect of the short-wavelength acoustic modes may not be important for the ferroelectric phase transition. If the homogeneous strain is frozen at zero, however, we find a direct cubic–rhombohedral phase transition, instead of the correct series of three transitions. This demonstrates the important role of homogeneous strain.

Second, we studied the significance of the long-range Coulomb interaction in the simulation. To do this, we changed the effective charge of the local mode (and thus the dipole–dipole interaction strength), while modifying the second-order self-energy parameter  $\kappa_2$ , so that the frequencies of the zone-center and zone-boundary modes remain in agreement with the LDA values. We found only a slight change (10%) of the transition temperatures when the dipole–dipole interaction strength was doubled. However, elimination of the dipole–dipole interaction altogether changed the results dramatically; the ground state becomes a complex antiferroelectric structure similar to the room-temperature structure of  $\text{PbZrO}_3$ . This result shows that it is essential to include the long-range interaction, although small inaccuracies in the calculated values of the effective charges or dielectric constants may not be very critical.

Third, we investigated the sensitivity of our results to variations of the short-range interaction parameters. We find the accuracy of the first-neighbor interaction parameters ( $j_1, j_2$ ) is very important, and a mere 10% deviation can change the calculated transition temperatures dramatically, and can sometimes even change the ground state structure. Second nearest-neighbor interactions are less important, and for the third-neighbor interactions,

even a 100% change does not seem to have a strong effect on the values of  $T_c$ . This result is to be expected, and partly justifies our choice of including only up to third neighbors for the short range interactions. We have also tested the effect of our assumption  $j_6 - 2j_7 = 0$ . We find that any reasonable choice leads to a barely noticeable change in  $T_c$ .

In short, highly accurate LDA calculations do appear to be a prerequisite for an accurate determination of the transition temperatures, but as long as certain features of the energy surface are correctly described, other approximations can be made without significantly affecting the results.

## VI. CONCLUSIONS

We have developed a first-principles approach to the study of structural phase transitions and finite-temperature properties in perovskite compounds. We construct an effective Hamiltonian based on Taylor expansion of the energy surface around the cubic structure, including soft optical modes and strain components as the possible distortions. The expansion parameters are determined by first-principles density-functional calculations using Vanderbilt's ultra-soft pseudopotential.

We have applied this scheme to  $\text{BaTiO}_3$  and calculated the pressure-temperature phase diagram. We have obtained the sequence of low-temperature phases, the transition temperatures, and the spontaneous polarizations, and found them to be in good agreement with experiment. We find that long-wavelength acoustic modes and long-range dipolar interactions both play an important role in the phase transition, while short-wavelength acoustic modes are not as significant. Accurate LDA calculations are required for accurate determination of the transition temperatures. The C-T phase transition is not found to be well described as a simple displacive transition; on the contrary, if anything it has more order-disorder character.

With slight modifications, our approach should be applicable to other perovskite compounds, as long as their structure is close to cubic and there are some low energy distortions

responsible for the phase transitions. It can be easily applied to ferroelectric materials like  $\text{PbTiO}_3$  (under study by another group<sup>14</sup>) and  $\text{KNbO}_3$ . It can also be applied to antiferroelectric materials like  $\text{PbZrO}_3$ . The application to antiferrodistortive materials like  $\text{SrTiO}_3$  is slightly more involved, though also successful.<sup>33</sup>

#### **ACKNOWLEDGMENTS**

We would like to thank R.D. King-Smith, U. V. Waghmare, R. Resta, Z. Cai, and A.M. Ferrenberg for useful discussions. This work was supported by the Office of Naval Research under contract number N00014-91-J-1184 and N00014-91-J-1247.

## REFERENCES

<sup>1</sup> M. E. Lines and A. M. Glass, *Principles and Applications of Ferroelectrics and Related Materials*, (Clarendon Press, Oxford, 1977).

<sup>2</sup> M. T. Dove, A. P. Giddy, and V. Heine, *Ferroelectrics* **136**, 33 (1992).

<sup>3</sup> E. Pytte, *Phys. Rev. B* **5**, 3758 (1972).

<sup>4</sup> A. D. Bruce and R. A. Cowley, *Structural Phase Transitions*, (Taylor & Francis, London, 1981).

<sup>5</sup> H. Bilz, G. Benedek, and A. Bussmann-Holder, *Phys. Rev. B* **87**, 4840 (1987) and references therein.

<sup>6</sup> G. Gordon and Y. S. Kim, *J. Chem. Phys.* **56**, 3122 (1972); L. L. Boyer *et al*, *Phys. Rev. Lett.* **54**, 1940 (1985); P. J. Edwardson *et al*, *Phys. Rev. B* **39**, 9738 (1989).

<sup>7</sup> R. E. Cohen and H. Krakauer, *Phys. Rev. B* **42**, 6416 (1990); R. E. Cohen and H. Krakauer, *Ferroelectrics* **136**, 65 (1992); R. E. Cohen, *Nature* **358**, 136 (1992).

<sup>8</sup> D. J. Singh and L. L. Boyer, *Ferroelectrics* **136**, 95 (1992).

<sup>9</sup> R. D. King-Smith and D. Vanderbilt, *Ferroelectrics* **136**, 85 (1992).

<sup>10</sup> R. D. King-Smith and D. Vanderbilt, *Phys. Rev. B* **49**, 5828 (1994).

<sup>11</sup> R. D. King-Smith and D. Vanderbilt, *Phys. Rev. B* **47**, 1651 (1993); D. Vanderbilt and R. D. King-Smith, *Phys. Rev. B* **48**, 4442 (1993).

<sup>12</sup> W. Zhong, R. D. King-Smith and D. Vanderbilt, *Phys. Rev. Lett.* **72**, 3618 (1994).

<sup>13</sup> K. M. Rabe and J. D. Joannopoulos, *Phys. Rev. Lett.* **59**, 570 (1987); *Phys. Rev. B* **36**, 6631 (1987).

<sup>14</sup> K. M. Rabe and U. V. Waghmare, to be published in *Ferroelectrics*.

<sup>15</sup> D. Vanderbilt, *Phys. Rev. B* **41**, 7892 (1990).

<sup>16</sup> W. Zhong, D. Vanderbilt, and K.M. Rabe, Phys. Rev. Lett. **73**, 1861 (1994).

<sup>17</sup> K. M. Rabe and U. V. Waghmare, unpublished.

<sup>18</sup> D. Vanderbilt, S.H. Taole, and S. Narasimhan, Phys. Rev. B **40**, 5657 (1989); B **42**, 11373(E) (1990).

<sup>19</sup> M. P. Allen and D. J. Tildesley, *Computer Simulation of Liquids* (Oxford, New York, 1990).

<sup>20</sup> P. N. Keating, Phys. Rev. **145**, 637 (1966).

<sup>21</sup> M.C. Payne, M.P. Teter, D.C. Allan, T.A. Arias, and J.D. Joannopoulos, Rev. Mod. Phys. **64** 1045 (1992).

<sup>22</sup> T.A. Arias, M.C. Payne and J.D. Joannopoulos, Phys. Rev. Lett. **69**, 1077 (1992).

<sup>23</sup> H.J. Monkhorst and J.D. Pack, Phys. Rev. B **13**, 5188 (1976).

<sup>24</sup> K. Binder and D. W. Heermann, *Monte Carlo Simulation in Statistical Physics* (Springer-Verlag, Berlin, 1988); K. Binder, ed. *The Monte Carlo Method in Condensed Matter Physics*, (Springer-Verlag, Berlin, 1992); K. Binder ed. *Application of the Monte Carlo Method in Statistical Physics*, (Springer-Verlag, Berlin, 1984).

<sup>25</sup> N. Metropolis et. al, J. Chem. Phys. **21**, 1087 (1953).

<sup>26</sup> A. M. Ferrenberg and R. H. Swendsen, Phys. Rev. Lett. **61**, 2635 (1988); **63**, 1195 (1989); J. Lee and J. M. Kosterlitz, Phys. Rev. Lett. **65**, 137 (1990); Phys. Rev. B **43**, 3265 (1991);

<sup>27</sup> T. Mitsui *et al.*, *Landolt-Bornstein numerical data and functional relationships in science and technology* (Springer-Verlag, 1981), NS, III/**16**; E. Nakamura *et al.*, *ibid.* NS, III/**28**.

<sup>28</sup> R. Clarke and L. Benguigui, J. Phys. C **10**, 1963 (1977).

<sup>29</sup> G. Samara, Phys. Rev. **151**, 378 (1966).

<sup>30</sup> H. H. Wieder, Phys. Rev. **99**, 1161 (1955).

<sup>31</sup> W. Janke, Phys. Rev. B **47**, 14757 (1993).

<sup>32</sup> Under a *physical* applied pressure, the latent heat would be the change of enthalpy, not energy. If this were applied to our case of a *fictitious* pressure, the calculated latent heats would be approximately twice as large.

<sup>33</sup> W. Zhong and D. Vanderbilt, Phys. Rev. Lett., in press.

TABLES

TABLE I. The energy per 5-atom unit cell (excluding the dipole energy) in terms of intersite interaction parameters of Fig. 2, for configurations shown in Fig. 3.

Configuration	expression
(a)	$\kappa_2 + 2j_1 + j_2 + 4j_3 + 2j_4 + 4j_6$
(b)	$\kappa_2 + 2j_1 - j_2 - 4j_3 + 2j_4 - 4j_6$
(c)	$\kappa_2 + j_2 - 2j_4 - 4j_6$
(d)	$\kappa_2 - 2j_1 + j_2 - 4j_3 + 2j_4 + 4j_6$
(e)	$\kappa_2 + j_2 - 2j_4 + 4j_6$
(f)	$\kappa_2 - 2j_1 - j_2 + 4j_3 + 2j_4 - 4j_6$
(g)	$\kappa_2/2 + j_1 - 2j_5 - 4j_7$

TABLE II. Expansion parameters of the Hamiltonian for BaTiO<sub>3</sub>. Energies are in Hartrees.

On-site	$\kappa_2$	0.0568	$\alpha$	0.320	$\gamma$	-0.473
Intersite	$j_1$	-0.02734	$j_2$	0.04020		
	$j_3$	0.00927	$j_4$	-0.00815	$j_5$	0.00580
	$j_6$	0.00370	$j_7$	0.00185		
Elastic	$B_{11}$	4.64	$B_{12}$	1.65	$B_{44}$	1.85
Coupling	$B_{1xx}$	-2.18	$B_{1yy}$	-0.20	$B_{4yz}$	-0.08
Dipole	$Z^*$	9.956	$\epsilon_\infty$	5.24		

TABLE III. Calculated transition temperatures  $T_c$ , saturated spontaneous polarizations  $p_s$ , and estimated latent heats  $l$ , as a function of simulation cell size.

	phase	$L = 10$	$L = 12$	$L = 14$	expt <sup>a</sup>
$T_c$ (K)	O–R	197±3	200±10	200±5	183
	T–O	230±10	232±2	230±10	278
	C–T	~290	296±1	297±1	403
$p_s$ (C/m <sup>2</sup> )	R	0.43	0.43	0.43	0.33
	O	0.35	0.35	0.35	0.36
	T	0.28	0.28	0.28	0.27
$l$ (J/mol)	O–R	50	60	60	33–60
	T–O	90	90	100	65–92
	C–T	–	–	150	196–209

<sup>a</sup>Ref. 27

## FIGURES

FIG. 1. The structure of the cubic perovskite compound  $\text{BaTiO}_3$ . Ba, Ti and O atoms are represented by shaded, solid, and empty circles respectively. Lengths of the vectors indicate the relative magnitudes of the displacements for a local mode polarized along  $\hat{\mathbf{x}}$ .

FIG. 2. The independent intersite interactions corresponding to the parameters  $j_1, j_2$  (first neighbor),  $j_3, j_4, j_5$  (second neighbor), and  $j_6$  and  $j_7$  (third neighbor).

FIG. 3. The local mode arrangements for which first-principles total-energy calculations were performed to determine the intersite interaction parameters. The arrangements can be labeled by the wavevector  $\mathbf{k}$  and a polarization vector ( $\hat{\mathbf{p}}$ ). The arrows represent local mode vectors. The dotted lines indicate the unit cells of the simple cubic lattice. The solid lines show the supercells used in the calculations. (a)  $\Gamma, \hat{\mathbf{p}} = \hat{\mathbf{z}}$  ; (b)  $X, \hat{\mathbf{p}} = \hat{\mathbf{z}}$  ; (c)  $X, \hat{\mathbf{p}} = \hat{\mathbf{x}}$  ; (d)  $M, \hat{\mathbf{p}} = \hat{\mathbf{z}}$  ; (e)  $M, \hat{\mathbf{p}} = \hat{\mathbf{x}}$  ; (f)  $R, \hat{\mathbf{p}} = \hat{\mathbf{z}}$  ; (g) four-cell calculation.

FIG. 4. The averaged largest, middle, and smallest components  $u_1, u_2, u_3$  and amplitude  $u$  of local modes as a function of temperature in the cooling-down simulation of a  $12 \times 12 \times 12$  lattice described in Section IV. The dotted lines are guides to the eye.

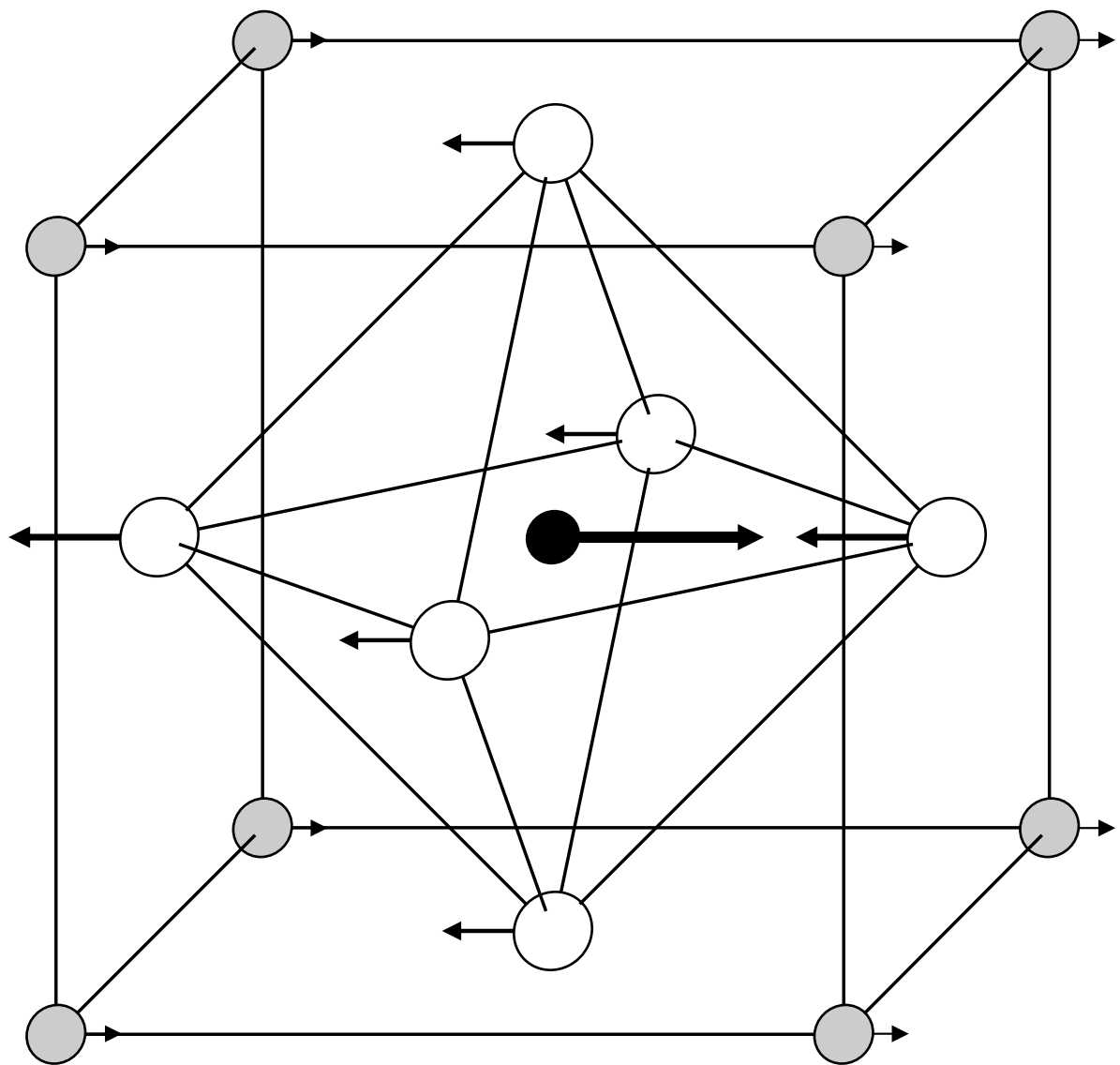
FIG. 5. The averaged homogeneous strain  $\eta_H$  as a function of temperature in the cooling-down simulation of a  $12 \times 12 \times 12$  lattice described in Section IV. The strains are measured relative to the LDA minimum-energy cubic structure with lattice constant 7.46 au. The dotted lines are guides to the eye.

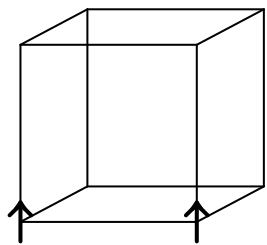
FIG. 6. The calculated pressure-temperature phase diagram. The cubic-tetragonal (C-T), tetragonal-orthorhombic (T-O) and orthorhombic-rhombohedral (O-R) transitions are labeled by solid triangles, circles and squares, respectively. The vertical dash-dot line at  $P = -4.8$  GPa corresponds to zero pressure in the experiment to compensate for the LDA volume error.

FIG. 7. The probability distribution of the Cartesian component of the local mode variable  $u_x$  in the cubic phase at  $T = 320\text{K}$  (solid line),  $350\text{K}$  (dashed line), and  $500\text{K}$  (dotted line).

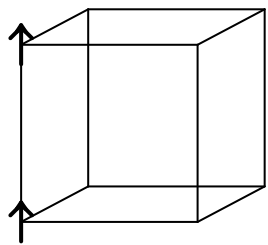
FIG. 8. Temperature dependence of squared eigenfrequency  $\omega^2$  at  $\mathbf{k} = (\pi/4a, \pi/4a, 0)$  for (a) LO, (b) TO1, and (c) TO2 modes.

FIG. 9. Calculated mode hardness quantity  $\rho(\mathbf{k})$ , Eq. (15), along special directions in the Brillouin zone.

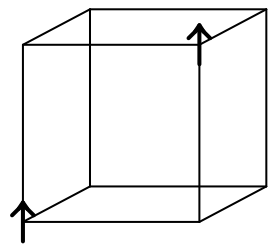




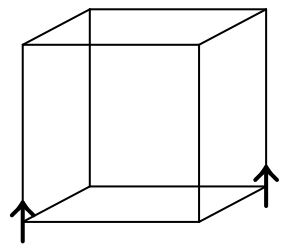
$j_1$



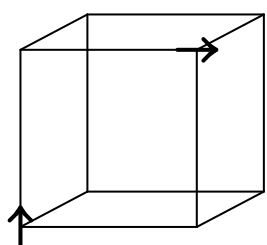
$j_2$



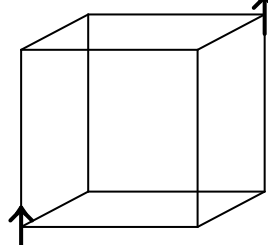
$j_3$



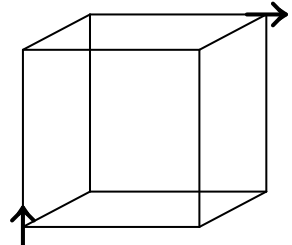
$j_4$



$j_5$



$j_6$



$j_7$

